Adjoint-Based Mesh Adaptation for the Sonic Boom Signature Loudness

Sriram K. Rallabhandi[*] and Michael A. Park[†]

NASA Langley Research Center, Hampton, Virginia, 23681

The mesh adaptation functionality of FUN3D is utilized to obtain a mesh optimized to calculate sonic boom ground signature loudness. During this process, the coupling between the discrete-adjoints of the computational fluid dynamics tool FUN3D and the atmospheric propagation tool sBOOM is exploited to form the error estimate. This new mesh adaptation methodology will allow generation of suitable meshes adapted to reduce the estimated errors in the ground loudness, which is an optimization metric employed in supersonic aircraft design. This new output-based adaptation could allow new insights into meshing for sonic boom analysis and design, and complements existing output-based adaptation techniques such as adaptation to reduce estimated errors in off-body pressure functional. This effort could also have implications for other coupled multidisciplinary adjoint capabilities (e.g., aeroelasticity) as well as inclusion of propagation specific parameters such as prevailing winds or non-standard atmospheric conditions. Results are discussed in the context of existing methods and appropriate conclusions are drawn as to the efficacy and efficiency of the developed capability.

I.   Introduction and Motivation

Interest in developing business jets[1,2] and larger[3,4] classes of commercial supersonic vehicles has driven sonic boom analysis and mitigation research over the past half century. During the last decade, there have been renewed efforts to push the state-of-the-art in computational methods and analyses tools that improve numerical modeling and offer new insights into the design process. Supersonic flight over land, which is currently prohibited,[5] is critical to the success of future commercial supersonic aircraft. Accurately modeling and improving the acceptability of sonic boom is critical to providing impetus to support replacement of this prohibition policy with a certification standard.

Loudness and annoyance are inherently subjective measures of the sonic boom experience that impact acceptability. Many noise descriptors have been evaluated as loudness predictors in human experiments, for example see Leatherwood et al.[6] The Mark VII perceived level (PL) of Stevens[7] is correlated with loudness and annoyance in multiple experiments.[6] While it is desirable to use the PL as the ground level metric to perform adjoint-based mesh adaptation, it's calculation is not amenable to differentiation, which is a pre-requisite in adjoint-based analysis. A surrogate of PL, the A-weighted sound exposure level (ASEL), is used in this study because of its continuous formulation that supports sensitivity analysis in both the time and frequency domains. ASEL is a good surrogate for PL of outdoor booms because it is also highly correlated to human response data[8] and has a similar frequency weighting.

Evaluation of the loudness footprint of an aircraft concept flying at supersonic speeds involves a multi-step process (see Fig. 1(a)) that begins by calculating the pressure field around an aircraft using a Computational Fluid Dynamics (CFD) solver, such as FUN3D.[9] A near-field pressure waveform, usually offset from the body by 2 or 3 body-lengths, is extracted from the CFD solution and propagated to the ground using an augmented Burgers solver sBOOM.[10] The ASEL and PL noise measures are calculated from the ground signature. A discrete-adjoint formulation for this process has been created for design optimization,[11] where the coupling between CFD and propagation tools allows computation of ASEL sensitivities to underlying mesh and geometry parameters, see Fig. 1(b).

---

[*]Aerospace Engineer, Aeronautics Systems Analysis Branch, Systems Analysis and Concepts Directorate, MS 442, AIAA Associate Fellow

[†]Research Scientist, Computational Aerosciences Branch, Research Directorate, MS 128, Senior Member AIAA
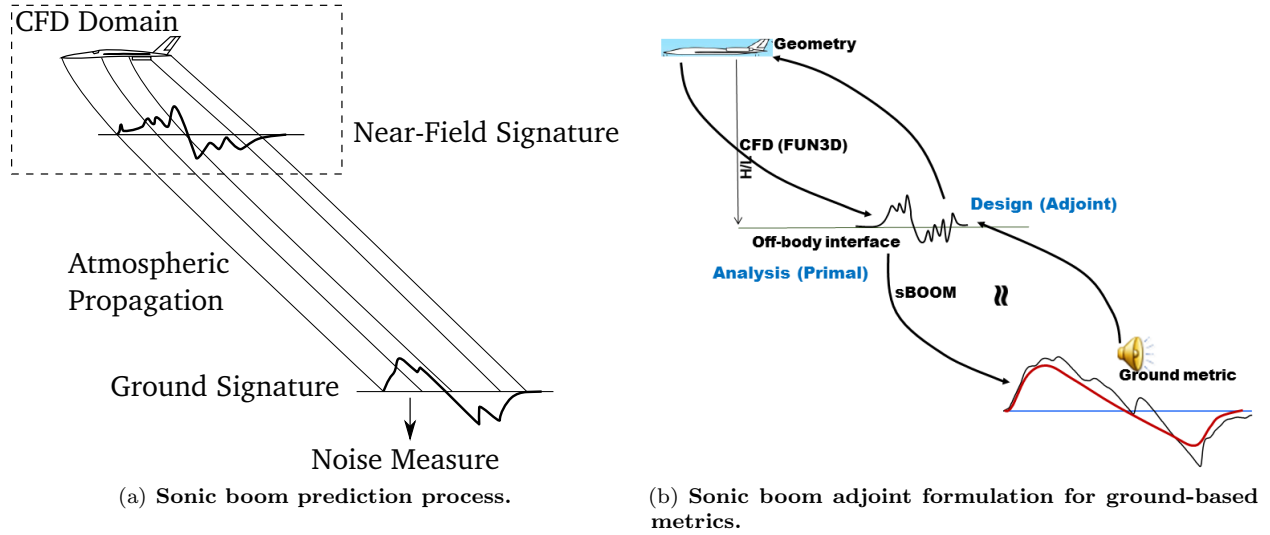
American Institute of Aeronautics and Astronautics

(a) **Sonic boom prediction process.**

(b) **Sonic boom adjoint formulation for ground-based metrics.**

Figure 1. **Multidisciplinary analysis and adjoint process for sonic boom noise measure.**

The CFD mesh is a critical element of the CFD analysis portion of the coupled formulation in Fig. 1. Park et al.[12] reviews specialized grid methods that have been developed to calculate near-field pressure waveforms for sonic boom analysis. These methods have been shown to be accurate for simple configurations but can introduce an unacceptable level of variation for more complex and realistic vehicles,[13] especially as the corresponding sonic boom loudness metrics get lower. The static mesh approach is particularly prone to variation in the aft portion of the near-field, which is exacerbated by complex flow-field interactions and possible propulsion and plume effects. As design progresses further into preliminary design, it is important to capture the underlying physics with progressively higher fidelity.

While feature-based mesh adaptation has been used in the literature, using output-based mesh adaptation becomes a crucial step to obtain a suitable mesh for the objective being optimized in a quantifiable and mathematically rigorous process. There have been multiple instances where the improvements gained with design optimization on prescribed meshes are not realized when the mesh describing the optimized configuration is adapted to reduce error. Ref. [14] highlights the importance of mesh adaptation during the design process.

Output-error estimates based on adjoint analysis help to address these problems by quantifying how local residual errors impact a specified output, and accounting for propagation effects in the process.[14] The resulting error estimate can be used to determine if the engineering output has been computed to sufficient accuracy, and to drive an adaptive method when the output error is greater than a user-specified tolerance. Additionally, adapting the grid to improve the same functional as the design optimization yields improvements that are not corrupted with estimated discretization error.[15]

II.   Background

In the context of output-based mesh adaptation for sonic boom analysis and design, earlier studies have used off-body (dpp) pressure targets to achieve mesh convergence. Nemec, Aftosmis, and Wintzer[16] use the integral of quadratic pressure deviation over a line segment (l) in the domain as in Eq. 1, where p and p_∞ denote the actual and ambient pressures respectively.

$$f = \int_l \left(\frac{p - p_\infty}{p_\infty} \right)^2 \, \mathrm{d}l. \tag{1}$$

This function reduces the discretization error in the pressure calculation along this prescribed line. Previous applications have been performed with the integral of pressure deviation over a surface.[17–19] However, the square of this deviation has been shown to produce more accurate signatures with fewer control volumes.[16] The integral extent can be restricted to a region of interest in the near-field signature to visualize the portion of the geometry and flow-field that impact this region of the signature.[20,21] The success of this method for Euler CFD was demonstrated at the 2008 NASA Fundamental Aeronautics Program Sonic Boom Prediction

Workshop, where two independent output-based adaptation schemes produced equivalent (grid converged) near-field signatures.[22]

Despite earlier success using near-field target pressure deviation for mesh adaptation (dpp adaptation), this is only a heuristic when the analysis and control of the ASEL ground noise measure is the objective. Using the adjoint-based methodology for ASEL eliminates the assumption of the quadratic pressure integral and its emphasis on the largest pressure deviations from ambient pressures and improves the accuracy of ASEL by appropriately refining the mesh using coupled, multi-disciplinary sonic boom analysis. Improvements demonstrated by mesh adaptation to control estimated error in ASEL may also be applied to other multidisciplinary analyses (e.g., aero-acoustics and aero-propulso-servo-elasticity[23,24]).

III. Methodology

FUN3D[9,25] is a node-based finite-volume unstructured Navier-Stokes solver that solves the equations on mixed element grids, including tetrahedra, pyramids, prisms, and hexahedra. The code also has a two-dimensional capability exercised in this work for triangular grids. FUN3D has been coupled to the augmented Burgers equation solver sBOOM.[10] A more detailed description of the adjoint-based formulation in sBOOM is given by Rallabhandi.[26] An adjoint formulation for this analysis process has been created for design optimization[11] and is also used for mesh adaptation.

The current output-based adaptation method is based on the 2D output-based error estimation and adaptation scheme developed by Venditti,[27] which utilized an embedded grid and developed a procedure to calculate a new grid spacing request from the adaptive indicator and a user specified error tolerance. This method has been implemented in 3D[28] within a parallel[17] framework for use with FUN3D flow and discrete adjoint solutions. The anisotropy of mesh elements is based on the Mach Hessian (M), where the element size in the smallest spacing direction is dictated by the output-based new grid spacing request. The anisotropic spacing request is specified by scaling the metric M to match the smallest spacing direction of the output-based request. A constant-complexity scaling[29] is applied to M to allow the user to directly specify the size of the adapted grid. This approach optimizes the grid at a fixed mesh size. The local elemental operators of node insertion, node movement, element swap, and element collapse are utilized to iteratively drive the edge lengths to unity in M. This implementation has been verified by comparison to alternative implementations.[30]

IV. Numerical Results

The following sections present the results of two adaptation mechanisms. The first is off-body pressure adaptation, which is synonymous to near-field pressure adaptation. The second is loudness adaptation, which is synonymously and interchangeably referred to as ASEL adaptation in this paper.

A. 2D Simulations

An Euler 2D airfoil is used to demonstrate the current coupled adjoint method and an existing near-field target pressure sonic boom prediction method. The first test case considered here is a simple 7 percent thick diamond airfoil with a chord of 100 feet in supersonic flow at a free-stream Mach number of 1.6, and zero angle of attack. The off-body pressure sensor is specified at 2 chords (or 200 feet) below the airfoil and the same location is used as the starting distance for propagation to the ground. The propagation uses an altitude of 45,000 feet, and US standard atmosphere with no winds is assumed. The airfoil and the initial mesh are shown in Fig. 2 along with the off-body sensor location at Z=-200.

Mesh adaptation is driven by an off-body pressure sensor, Eq. (1), and ground loudness objective, ASEL. The convergence of the remaining error estimate and noise measures is given in Fig. 3. For off-body pressure target Fig. 3(a) and ASEL Fig. 3(b) objectives, the remaining estimated error drops approximately three orders of magnitude. Both methods show a steady reduction in estimated error.

The convergence behavior of the noise measures PL and ASEL is slightly different for each mesh adaptation objective function. In this simple 2D case, the final values are almost identical for both ASEL and PL as shown in Fig. 3(c) and Fig. 3(d). However, this may not be true for more complex geometries of supersonic aircraft concepts. The ASEL and PL closely track each other for both cases indicating the validity of using ASEL as a surrogate for PL.
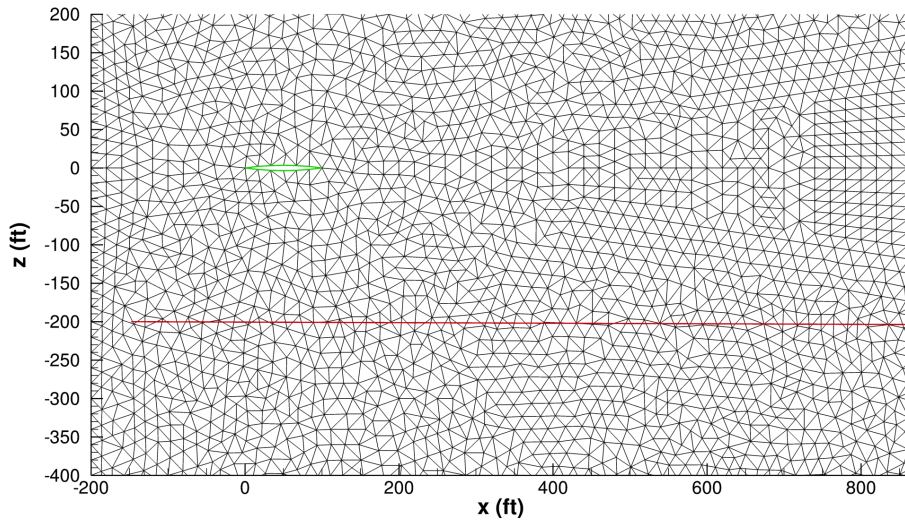
American Institute of Aeronautics and Astronautics

Figure 2. Initial CFD grid and near-field pressure extraction location.

The series of adapted meshes are shown in Fig. 4, where the axis units are in feet. The wake and areas aft of the tail shock were observed to be more refined when ground loudness was used as the adaptation objective, primarily because of higher sensitivity of ASEL to the near-field re-compression back to ambient conditions. As a result, there is additional mesh refinement further downstream compared to the traditional off-body pressure target case.

Because the mesh is allowed to increase in size to become highly refined; and because the underlying concept is fairly simple in that it produces 2 shocks and an expansion leading to an N-wave on the ground, no differences are observed between the two adaptation approaches in terms of sonic boom metrics. To delve deeper into the differences, two additional tests are run. Firs, the baseline mesh is made much coarser and the mesh size upper limit is constrained to see the impact on each of the adaptation techniques in extracting the shock flow-field. A second test involved using an airfoil that generates a complex near-field pressure waveform that produces a shaped low-boom ground signature.

A.1. Coarse Grid

A coarser initial mesh mesh, relative to the one in Fig. 2 followed by a less aggressive mesh growth factor is chosen to see how the two mesh adaptation schemes, one based on off-body pressure and the other based on ASEL, perform in terms of error and loudness metrics. The initial coarse mesh in Fig. 5 is approximately 8 times smaller than the mesh in Fig. 2. When using a refined initial mesh, unlike the off-body pressure functional, the ground-based ASEL functional seemed to refine the mesh farther into the wake as seen in Fig. 4(h), and this could cause the boundary conditions to affect the results. In order to alleviate any such problem and minimize the impact of the downstream boundary on the adaptation, the domain downstream was extended by 2.5 body lengths. As before, the adaptation was allowed to proceed 20 adaptation cycles and the results were compared.

Figure 6 compares the remaining error as a function of nodes. Although, the error functional is based on two different metrics and as such cannot be compared against each other directly, a few instructive details can be interpreted from this plot. First, the remaining error, for ground loudness adaptation reduces super-linearly $\mathcal{O}(h^2)$, where h is a measure of the cell size that is proportional to reciprocal of the number of nodes. The remaining error for the off-body pressure functional drops; however the convergence is flatter initially followed by a steeper reduction. Second, the remaining error estimate drops by three orders of magnitude for the ground loudness functional compared to two orders for the off-body functional for a similar size in the mesh growth guidance.

In the case of the ground loudness functional, no additional analysis is needed as the atmospheric propagation is wrapped in the adaptation process. For the off-body pressure functional, the near-field pressure waveform after each adaptation cycle is used as the starting waveform for propagation to the ground, and the loudness metrics are computed. Figure 7 compares the loudness convergence resulting from each adaptation
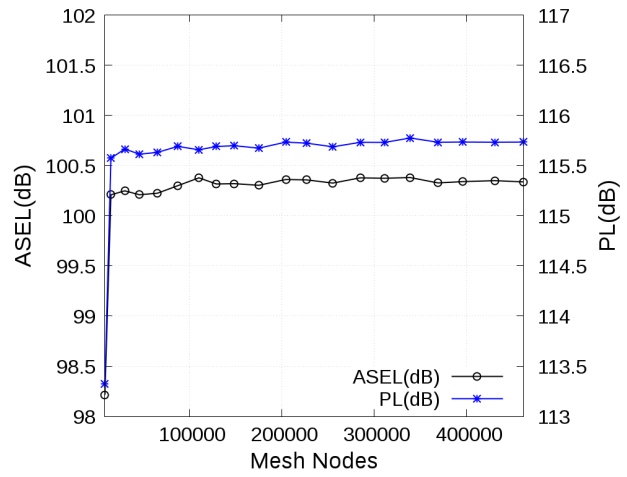
American Institute of Aeronautics and Astronautics
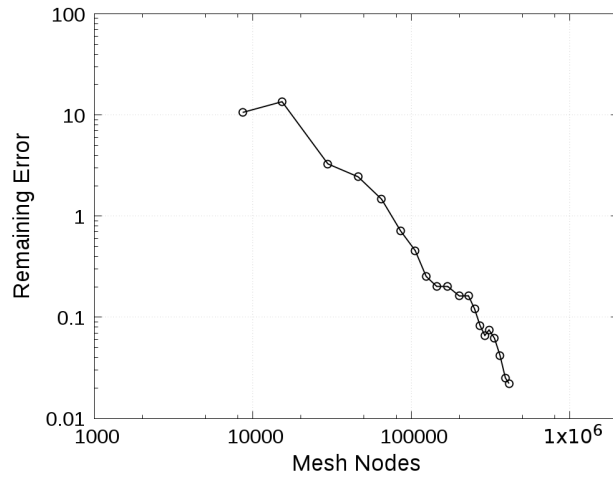
(a) **Off-body pressure functional remaining error estimate.**
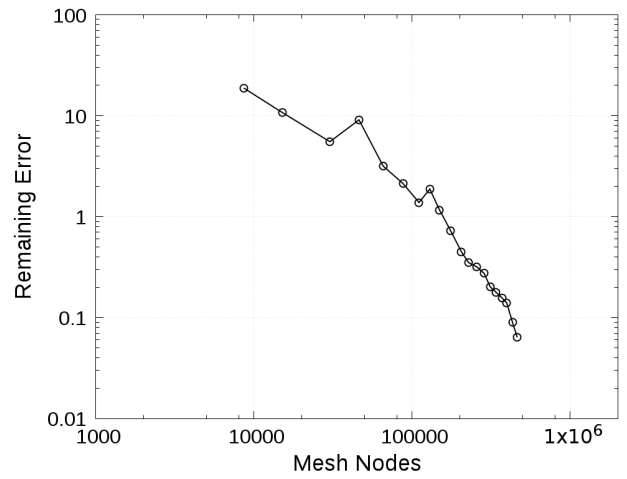
(b) **A-weighted loudness functional remaining error estimate.**
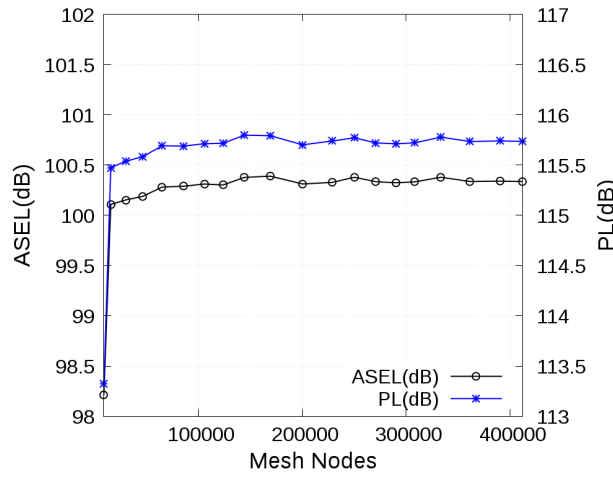
(c) **Loudness convergence: off-body pressure adaptation.**

(d) **Loudness convergence: ASEL adaptation.**

Figure 3. **Remaining error estimate and noise measure convergence during adjoint-based mesh adaptation.**

scheme. Since the initial mesh is coarser and the mesh growth is constrained to be nominal, slight differences are observed in the PL and ASEL metrics. Although, these difference could eventually be infinitesimal when more adaptation cycles are run; it is important to note that both schemes take a different path in reaching that result.

Figure 8 shows the evolution of the mesh through the different adaptation cycles. Because of the less aggressive mesh growth factors that were chosen, the meshes are much smaller compared to the meshes in Fig. 4 while producing almost the same loudness values at the ground. Just like the previous case, there is more refinement in the wake region, in the case of ASEL adaptation. The reason for this is that the ground loudness is sensitive to the waveform *close-out* to ambient conditions in the wake region. Another observation is that, using the ground objective tends to adapt regions above the geometry more than when using the off-body pressure objective, which at first seems counter-intuitive. However, since the waveform in the wake region is important for the ground loudness, and the wake depends on both the upper and lower regions of the geometry, the lower-surface bias of the off-body pressure functional is reduced when using the ground objective for adaptation. This could potentially be beneficial to address the uncertainty associated with the off-body location as three dimensional effects may not be completely resolved at the chosen location. Finally, the mesh is adapted farther into the domain using the ground objective than when using the near-field objective.

American Institute of Aeronautics and Astronautics

Figure 9 shows the initial near-field waveform and the final waveforms obtained using both adaptation mechanisms. While the final adapted near-fields look visually similar, subtle differences are observed near the shock locations and other regions of higher frequency content. The loudness adaptation does not aggressively resolve the high frequency sharp corners, particularly those that may not have an impact on the ground loudness. This can allow loudness-based adaptation to trade refinement at such locations with refinement in the wake and other smooth regions, which are not emphasized by the pressure-based functional.

Figure 10 shows the comparison of ground signatures for the two adaptation objectives, which have the classic N-wave shapes. For this simple 2D case, the results indicate a difference between the two adaptation approaches of 0.1 dB on the PL scale.

B. 2D Case with a Complex Flow-field

A more realistic and complex concept is needed to better understand the differences between the two adaptation mechanisms. Due to the high computational cost associated with mesh adaptation, a 2D analysis is desired. To satisfy these constraints, near-field waveform of a low boom demonstrator concept[31] is used in conjunction with linearized small perturbation theory to obtain the deflection angles corresponding to the pressure coefficient computed from the off-body pressure waveform. The deflection angles are integrated to obtain an airfoil profile. The under-track pressure waveform corresponding to low-boom concept from Ref. 14, and the resulting airfoil that is predicted to produce it are depicted in Fig. 11. This airfoil profile is then analyzed using FUN3D to see if the pressure waveform is realized using the adjoint-based mesh adaptation approaches.

Figure 12 depicts the contours of cell size metric, h_0, plotted at different adaptation cycles for both adaptation mechanisms. This term is computed by implying the metric from the current grid elements. The implied metric is averaged to the nodes from incident elements. The largest eigenvalue e of the average metric at the node is used to compute $h_0 = e^{-1/2}$. As the adaptation progresses, both schemes refine the mesh along the shocks and within the zone of influence directly beneath and behind the airfoil. However, subtle differences are observed between the two approaches. The ASEL adaptation refines the mesh and resolves the flow-field evenly in regions without strong shocks, particularly the last third of the airfoil, while off-body pressure adaptation aggressively goes after the highest deviations from the pressure target, which is zero for all the cases considered here.

Figure 13 shows the contours of the isotropic grid adaptation request. These contours show where each approach seeks to refine or coarsen the underlying mesh at that particular design cycle once the anisotropy has been established. By the fifth cycle, the ASEL adaptation has already started to resolve the mid-section of the region below the airfoil as it sees sensitivity and potential of the smaller shocks to coalesce with other shocks around them. The off-body pressure adaptation attempts to resolve the biggest shocks initially. ASEL adaptation attempts to resolve the aft portion of the domain evenly, whereas the off-body pressure functional ignores refinement in much of the aft except near the larger shocks. Finally, ASEL adaptation resolves the wake better than the off-body pressure adaptation.

Two different refinement levels are tested and compared in Figs. 14 and 15, where the obtained near-field pressure waveforms from each of the adaptation mechanisms using moderate and high mesh refinements are shown respectively. As expected, the larger shocks are resolved more sharply by off-body pressure adaptation, while ASEL adaptation attempts to resolve smaller shocks and fluctuations at appropriate locations that may have a higher sensitivity to the ground loudness metrics. The small pressure fluctuations in ranges $[170, 190]$ and $[205, 215]$ of figs. 14 and 15 are missed by the off-body pressure adaptation. Overlaid on these plots is the gradient of ASEL (plotted on a secondary Y-axis on the right) with respect to the near-field pressure waveform. Initially, the gradients are large showing that the solution is far from being converged. As the adaptation evolves, the gradient vector becomes more accurate and weighs appropriate portions of the signature based on ASEL sensitivity rather than pressure extrema used in off-body pressure adaptation. Two interesting observations can be made regarding these plots. First, the highest gradients may not be aligned with the shocks and this explains the differences observed during mesh adaptation using both approaches. Second, these gradients are noisy, particularly as the adaptation progresses due to the sampling of the waveform for propagation, leading to possible degradation in the ASEL adaptation. Future work will include an improved interpolation scheme to alleviate this issue. Despite the gradients being noisy, the norm continues to drcrease as the mesh adaptation progresses.

Figure 16(a) depicts the convergence history for each adaptation scheme and for three different mesh refinement levels. The remaining error trend is observed to be very similar between both schemes. Using a

refined grid allowed the remaining error to drop slowly and reach convergence asymptotically. The ground signatures and ASEL buildup are plotted in figs. 16(b) to 16(d). Using a coarse mesh is insufficient for both schemes in terms of computed PL. Both schemes converge to a similar PL using a refined mesh, however the ASEL adaptation reaches that PL using a moderately refined mesh, whereas the off-body pressure adaptation has slightly more error at the same mesh size. This shows that ASEL adaptation may be able to achieve loudness convergence faster and with smaller meshes than off-body pressure adaptation.

C.   3D Simulations Over a Demonstrator Concept

This section provides details on the application of adjoint-based mesh adaptation mechanisms described so far on a low-boom demonstrator concept. The starting mesh has approximately 31 million nodes, and Fig. 17 shows the baseline mesh, both under and aft of the concept. The starting mesh was generated using specialized meshing techniques for boom simulations.[12]

Adjoint mesh adaptation with a loudness metric is conducted for 8 cycles to achieve loudness convergence as seen in Fig. 18. The mesh size increases from about 31 million nodes to about 240 million nodes. The off-body pressure adaptation was then run for the same number of adaptation cycles to keep the meshes similar in size. After the adaptation is complete, the intermediate pressure waveforms are propagated to the ground and the ASEL values are plotted in Fig. 18. It is seen that, off-body pressure adaptation does not achieve the same convergence as ASEL adaptation for similar mesh sizes.

Figure 19 shows the off-body adapted meshes on the left and ASEL adapted meshes on the right. Both mechanisms adapt near the shocks, plume and wake regions, with subtle differences that are visually indistinguishable. The differences in the adaptation mechanisms become apparent when the near-field pressure waveforms corresponding to the adapted meshes are plotted as shown in Fig. 20. Both adaptation mechanisms reach a very different pressure profile than the baseline mesh. This again shows that a fixed mesh may not be able to resolve the near-field appropriately, even when using the best existing practices in generating specialized boom grids. The near-field waveforms from both adaptation mechanisms exhibit multiple subtle differences. Just like in the 2D cases, the off-body pressure adaptation resolves the larger peaks more sharply compared to the loudness adaptation. Smaller peaks and oscillations are captured by ASEL adaptation, while the off-body pressure adaptation misses and misplaces such smaller deviations, compared against ASEL adaptation, as it first attempts to resolve larger pressure deviations from the ambient conditions.

The corresponding ground signatures are plotted in Fig. 21, while the ASEL buildups are plotted on the secondary y-axis on the right. The ground signatures from both adaptations are significantly different from the signature resulting from the baseline mesh. Both adaptations produce under-track signatures that are very similar. However, the ASEL buildup plot reveals that the front portion of the signature from ASEL adaptation is steeper, and hence contributes more to loudness than that resulting from off-body pressure adaptation. The off-body adaptation recovers some of the loudness in the aft by having a slightly higher shock magnitude compared to the ASEL adaptation. Looking at the differences on the ASEL loudness scale (secondary y-axis), it may appear that the ground signature is closer to the baseline than to the signature from off-body pressure adaptation. As is evident from the ground signature figure, this is not true, and the proximity of the baseline and ASEL adaptation in terms of ASEL is fortuitous.

The adaptation mechanisms may also be compared by constraining the mesh size, similar to the exercise that was performed for the 2D case. However, it is omitted here for the sake of brevity. The primary take-away is that adjoint-based loudness adaptation offers an alternative approach to refine the mesh directly based on ground loudness metrics. Since computational resources are always limited, it is helpful if we can limit the mesh size while still capturing the key features in the near-field that can demonstrate loudness convergence. The existing off-body pressure adaptation technique typically refines large shocks, and without prior knowledge of the underlying concept for appropriate weighting, some of the smaller pressure deviations may be ignored initially. The effects of smaller shocks may only become important once the mesh is too large and further adaptation is impractical. The adjoint-based mesh adaptation driven by ground loudness provides this weighting implicitly based on acceptability metrics, rather than based on off-body pressure heuristics. It may be beneficial to study an adaptation mechanism that combines both off-body and loudness adaptations to achieve best of both approaches.

V.   Conclusions

Traditional output-based mesh adaptation processes for sonic boom have been focused on off-body (near-field) pressure waveforms or equivalent areas. This work enhances that adaptation to include ground loudness metrics by interfacing with an atmospheric propagation code and coupling adjoint sensitivities corresponding to pressure extrapolation with those from CFD to allow the mesh to be adapted for a boom acceptability criteria. This multidisciplinary approach has the following additional benefits: a) the mesh adaptation naturally refines regions in the wake and above the geometry to capture any plume or three dimensional effects, b) trades off mesh size in regions of importance to the ground loudness rather than for near-field pressure, which is a heuristic for sonic boom on the ground, and c) most importantly allows integration of the propagation analysis into the mesh adaptation process which may include non-standard atmospheric conditions such as presence of winds and humidity models. Results presented for two-dimensional and three-dimensional cases showed that the approach based on ground loudness is at-worst similar to the current state-of-the-art in terms of near-field pressure objective, while having the potential advantages in terms of adaptation metrics and loudness convergence measures. Additionally, the current ASEL loudness adaptation may be combined with off-body pressure adaptation to achieve a mesh that extracts useful features from both objectives.

Acknowledgments

References

[1]Henne, P. A., "Case for Small Supersonic Civil Aircraft," *AIAA Journal of Aircraft*, Vol. 42, No. 3, May–June 2005, pp. 765–774.

[2]Sakata, K., "Japan's Supersonic Technology and Business Jet Perspectives," AIAA Paper 2013–21, 2013.

[3]Magee, T. E., Wilcox, P. A., Fugal, S. R., Acheson, K. E., Adamson, E. E., Bidwell, A. L., and Shaw, S. G., "System-Level Experimental Validations for Supersonic Commercial Transport Aircraft Entering Service in the 2018-2020 Time Period, Phase I Final Report," NASA CR-2013-217797, Langley Research Center, Feb. 2013.

[4]Morgenstern, J., Norstrud, N., Sokhey, J., Martens, S., and Alonso, J. J., "Advanced Concept Studies for Supersonic Commercial Transports Entering Service in the 2018 to 2020 Period," NASA CR-2013-217820, Langley Research Center, Feb. 2013.

[5]"Civil Aircraft Sonic Boom," Code of Federal Regulations, Title 14, Pt. 91.817, 2011.

[6]Leatherwood, J. D., Sullivan, B. M., Shepherd, K. P., McCurdy, D. A., and Brown, S. A., "Summary of Recent NASA Studies of Human Response to Sonic Booms," *The Journal of the Acoustical Society of America*, Vol. 111, No. 1, Jan. 2002, pp. 586–598.

[7]Stevens, S. S., "Perceived Level of Noise by Mark VII and Decibels (E)," *Journal of the Acoustical Society of America*, Vol. 51, No. 2B, 1972, pp. 575–601.

[8]Loubeau, A., Naka, Y., Cook, B. G., Sparrow, V. W., and Morgenstern, J. M., "A New Evaluation of Noise Metrics for Sonic Booms Using Existing Data," *2nd International Sonic Boom Forum*, 20th International Symposium on Nonlinear Acoustics, July 2015.

[9]Biedron, R. T., Carlson, J.-R., Derlaga, J. M., Gnoffo, P. A., Hammond, D. P., Jones, W. T., Kleb, B., Lee-Rausch, E. M., Nielsen, E. J., Park, M. A., Rumsey, C. L., Thomas, J. L., and Wood, W. A., "FUN3D Manual: 13.0," NASA TM-2016-219330, Langley Research Center, Aug. 2016.

[10]Rallabhandi, S. K., "Advanced Sonic Boom Prediction Using the Augmented Burgers Equation," *AIAA Journal of Aircraft*, Vol. 48, No. 4, July–Aug. 2011, pp. 1245–1253.

[11]Rallabhandi, S. K., Nielsen, E. J., and Diskin, B., "Sonic Boom Mitigation Through Aircraft Design and Adjoint Methodology," *AIAA Journal of Aircraft*, Vol. 51, No. 2, March–April 2014.

[12]Park, M. A., Campbell, R. L., Elmiligui, A., Cliff, S. E., and Nayani, S. N., "Specialized CFD Grid Generation Methods for Near-Field Sonic Boom Prediction," AIAA Paper 2014–115, 2014.

[13]Park, M. A. and Morgenstern, J. M., "Summary and Statistical Analysis of the First AIAA Sonic Boom Prediction Workshop," *AIAA Journal of Aircraft*, Vol. 51, No. 2, March–April 2016, pp. 578–598.

[14]Fidkowski, K. J. and Darmofal, D. L., "Review of Output-Based Error Estimation and Mesh Adaptation in Computational Fluid Dynamics," *AIAA Journal*, Vol. 49, No. 4, April 2011, pp. 673–694.

[15]Nemec, M. and Aftosmis, M. J., "Output Error Estimates and Mesh Refinement in Aerodynamic Shape Optimization," AIAA Paper 2013–865, 2013.

[16]Nemec, M., Aftosmis, M. J., and Wintzer, M., "Adjoint-Based Adaptive Mesh Refinement for Complex Geometries," AIAA Paper 2008–725, 2008.

[17]Lee-Rausch, E. M., Park, M. A., Jones, W. T., Hammond, D. P., and Nielsen, E. J., "Application of a Parallel Adjoint-Based Error Estimation and Anisotropic Grid Adaptation for Three-Dimensional Aerospace Configurations," AIAA Paper 2005–4842, 2005.

[18]Jones, W. T., Nielsen, E. J., and Park, M. A., "Validation of 3D Adjoint Based Error Estimation and Mesh Adaptation for Sonic Boom Prediction," AIAA Paper 2006–1150, 2006.

[19]Park, M. A. and Darmofal, D. L., "Validation of an Output-Adaptive, Tetrahedral Cut-Cell Method for Sonic Boom Prediction," *AIAA Journal*, Vol. 48, No. 9, Sept. 2010, pp. 1928–1945.

[20]Park, M. A., *Anisotropic Output-Based Adaptation with Tetrahedral Cut Cells for Compressible Flows*, Ph.D. thesis, Massachusetts Institute of Technology, Sept. 2008.

[21]Aftosmis, M. J. and Nemec, M., "Cart3D Simulations for the First AIAA Sonic Boom Prediction Workshop," AIAA Paper 2014–558, 2014.

[22]Park, M. A., Aftosmis, M. J., Campbell, R. L., Carter, M. B., Cliff, S. E., and Bangert, L. S., "Summary of the 2008 NASA Fundamental Aeronautics Program Sonic Boom Prediction Workshop," *AIAA Journal of Aircraft*, Vol. 51, No. 3, May–June 2014, pp. 987–1001.

[23]Silva, W. A., Sanetrik, M. D., Chwalowski, P., Connolly, J., and Kopasakis, G., "Using FUN3D for Aeroelatic, Sonic Boom, and AeroPropulsoServoElastic (APSE) Analyses of a Supersonic Configuration," AIAA Paper 2016–1319, 2016.

[24]Connolly, J. W., Kopasakis, G., Chwalowski, P., Sanetrik, M. D., Carlson, J.-R., Silva, W. A., and McNamara, J., "Towards an Aero-Propulso-Servo-Elasticity Analysis of a Commercial Supersonic Transport," AIAA Paper 2016–1320, 2016.

[25]Anderson, W. K. and Bonhaus, D. L., "An Implicit Upwind Algorithm for Computing Turbulent Flows on Unstructured Grids," *Computers and Fluids*, Vol. 23, No. 1, 1994, pp. 1–22.

[26]Rallabhandi, S. K., "Sonic Boom Adjoint Methodology and its Applications," AIAA Paper 2011–3497, 2011.

[27]Venditti, D. A., *Grid Adaptation for Functional Outputs of Compressible Flow Simulations*, Ph.D. thesis, Massachusetts Institute of Technology, June 2002.

[28]Park, M. A., "Three–Dimensional Turbulent RANS Adjoint–Based Error Correction," AIAA Paper 2003–3849, 2003.

[29]Alauzet, F. and Loseille, A., "High-Order Sonic Boom Modeling Based on Adaptive Methods," *Journal of Computational Physics*, Vol. 229, No. 3, 2010, pp. 561–593.

[30]Park, M. A., Loseille, A., Krakos, J. A., and Michal, T., "Comparing Anisotropic Output-Based Grid Adaptation Methods by Decomposition," AIAA Paper 2015–2292, 2015.

[31]Wintzer, M., Ordaz, I., and Fenbert, J. W., "Under-track CFD-based Shape Optimization for a Low-Boom Demonstrator Concept," AIAA Paper 2015-2260, June 2015.
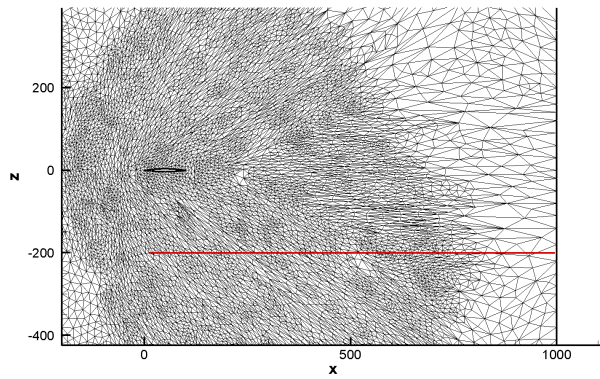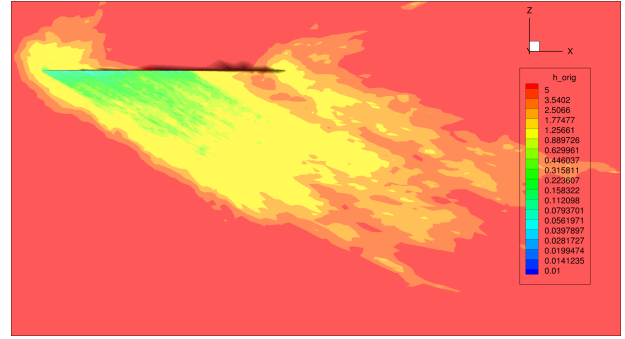
(a) **After the 1st off-body pressure adaptation cycle.**
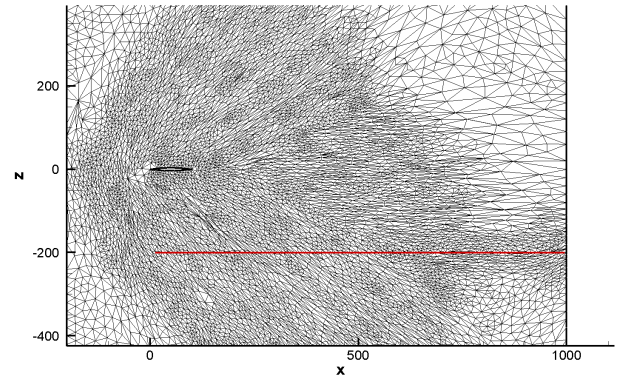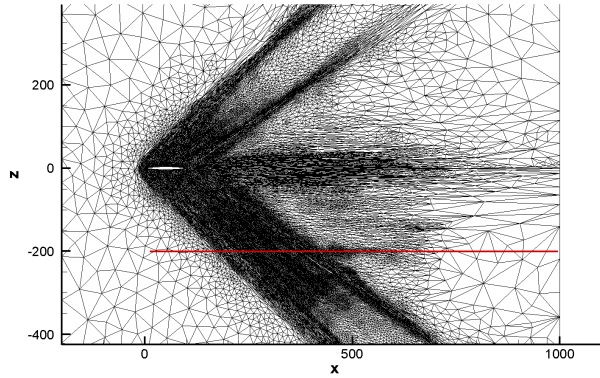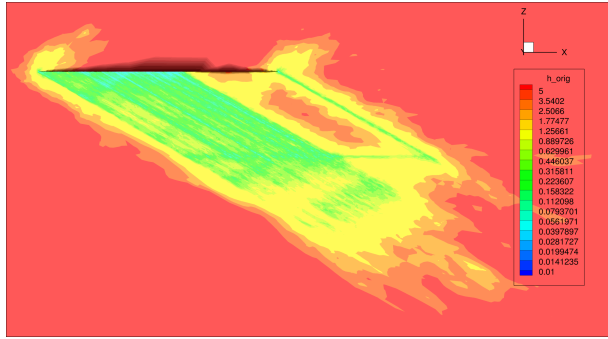
(b) **After the 1st ASEL adaptation cycle.**
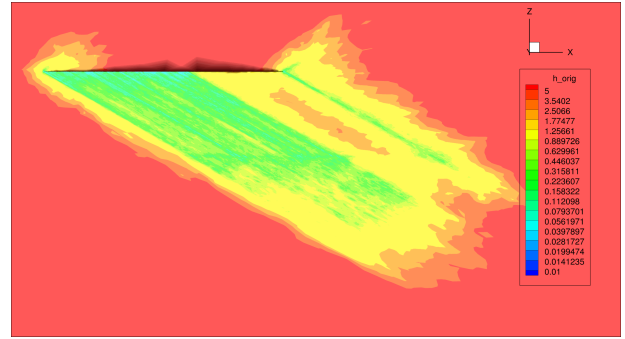
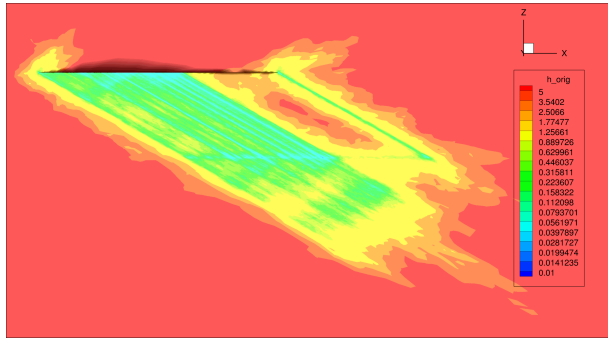(c) **After the 5th off-body pressure adaptation cycle.**
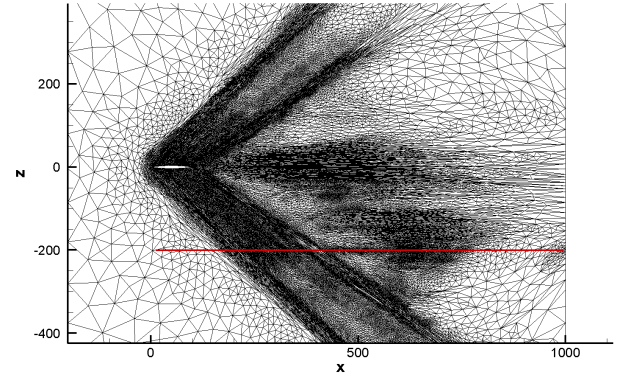
(d) **After the 5th ASEL adaptation cycle.**
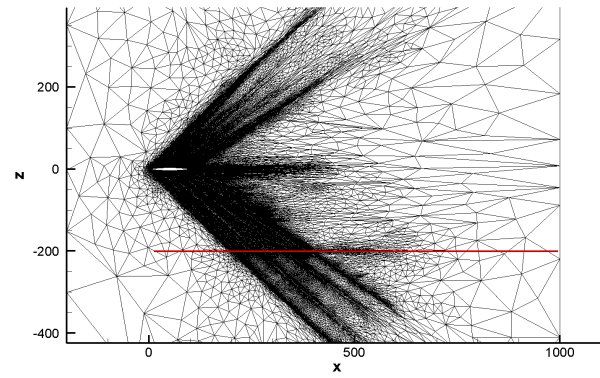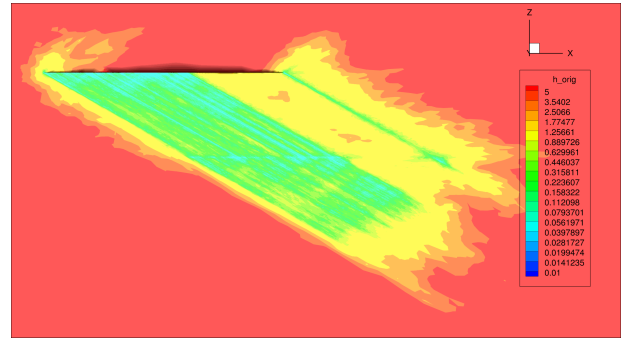
(e) **After the 10th off-body pressure adaptation cycle.**
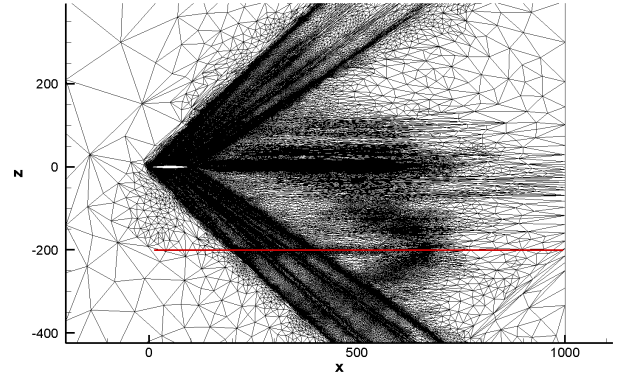
(f) **After the 10th ASEL adaptation cycle.**
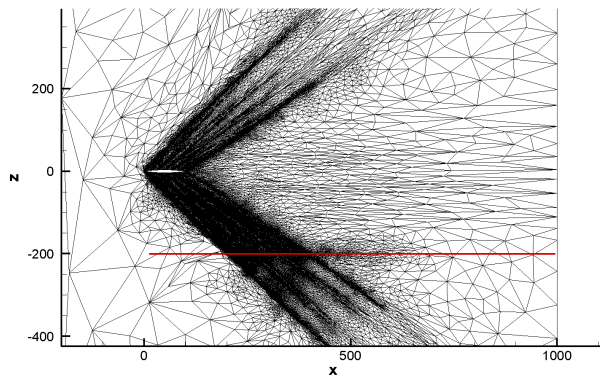
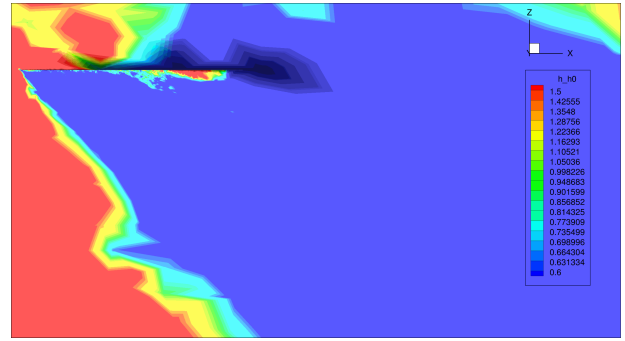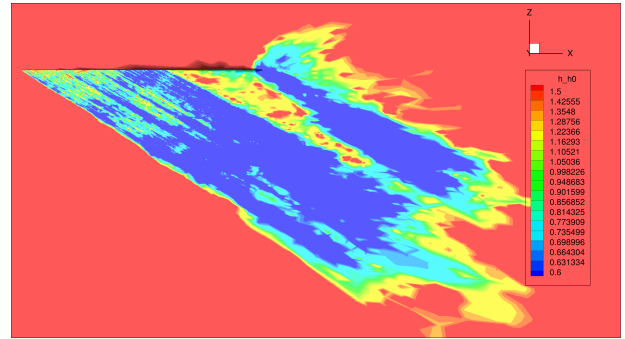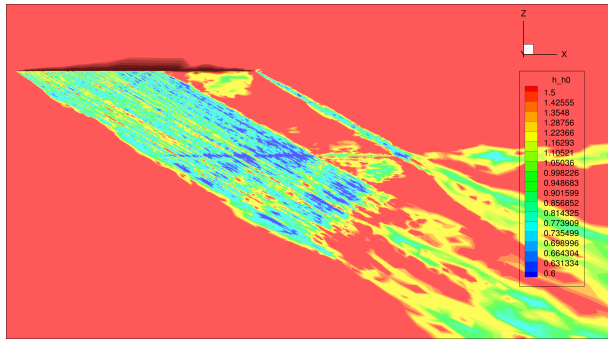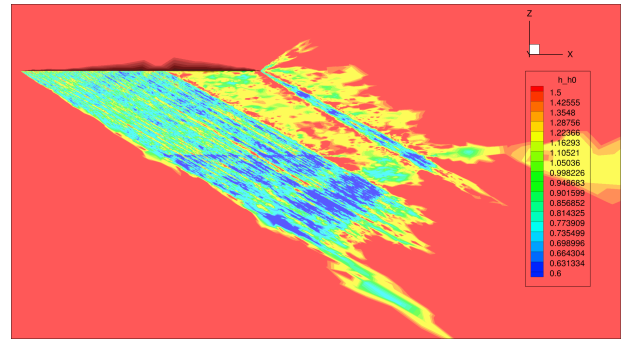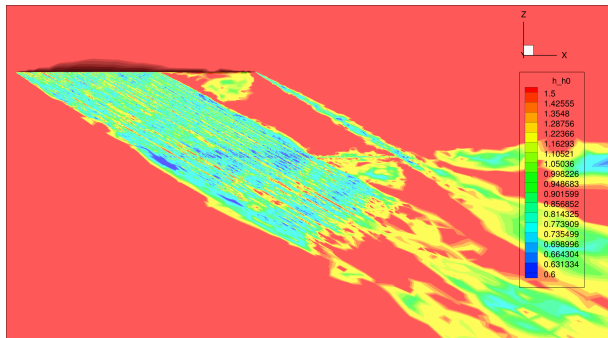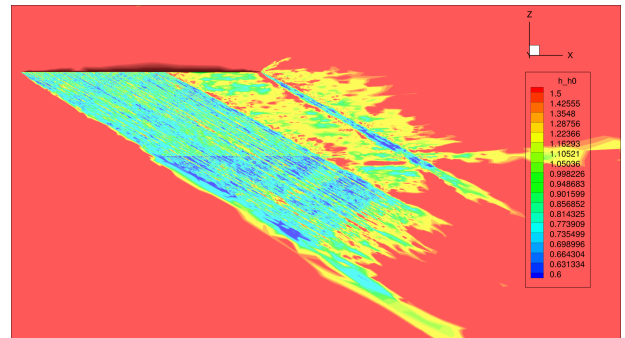(g) **After the 20th off-body pressure adaptation cycle.**
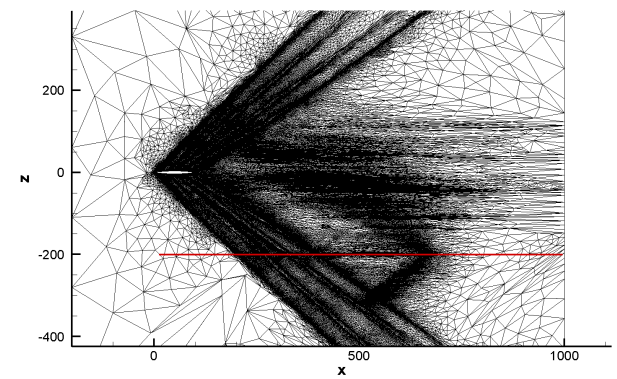
(h) **After the 20th ASEL adaptation cycle.**

Figure 4. Grid changes during adjoint-based mesh adaptation over a diamond airfoil with high refinement.
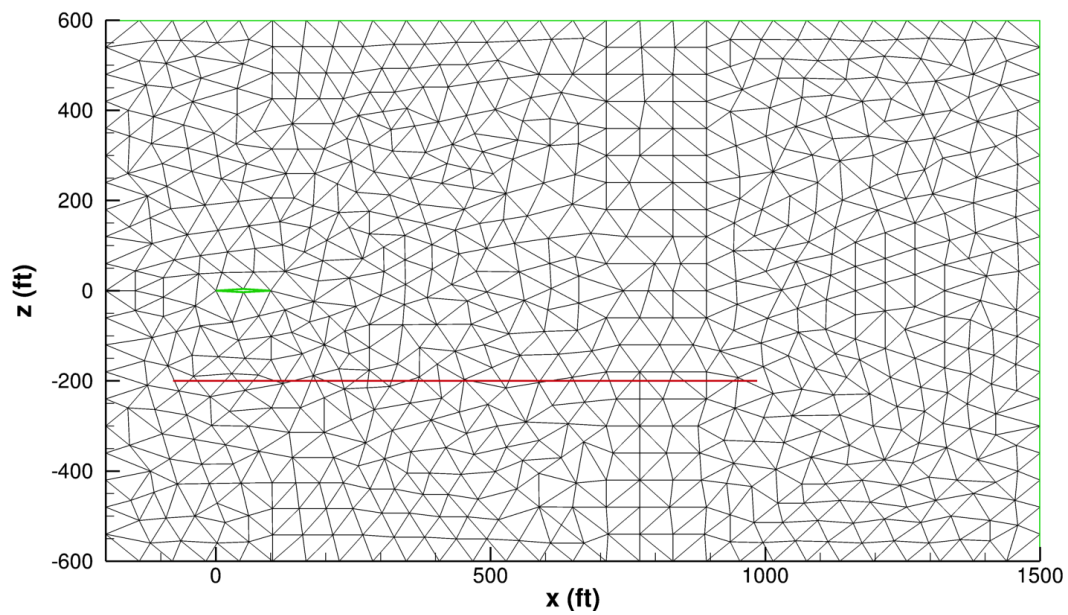
Figure 5. Initial coarse CFD grid and near-field pressure extraction location over a diamond airfoil.
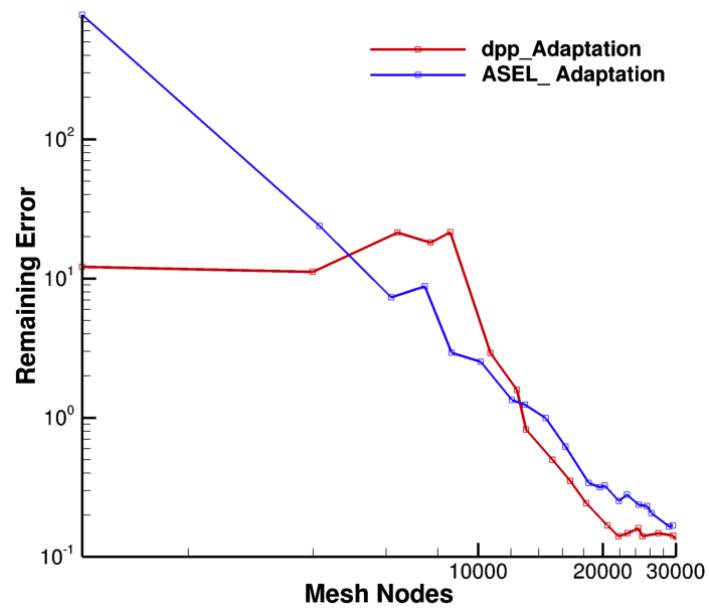
Figure 6. Remaining error estimate for each scheme for coarse meshes over a diamond airfoil.
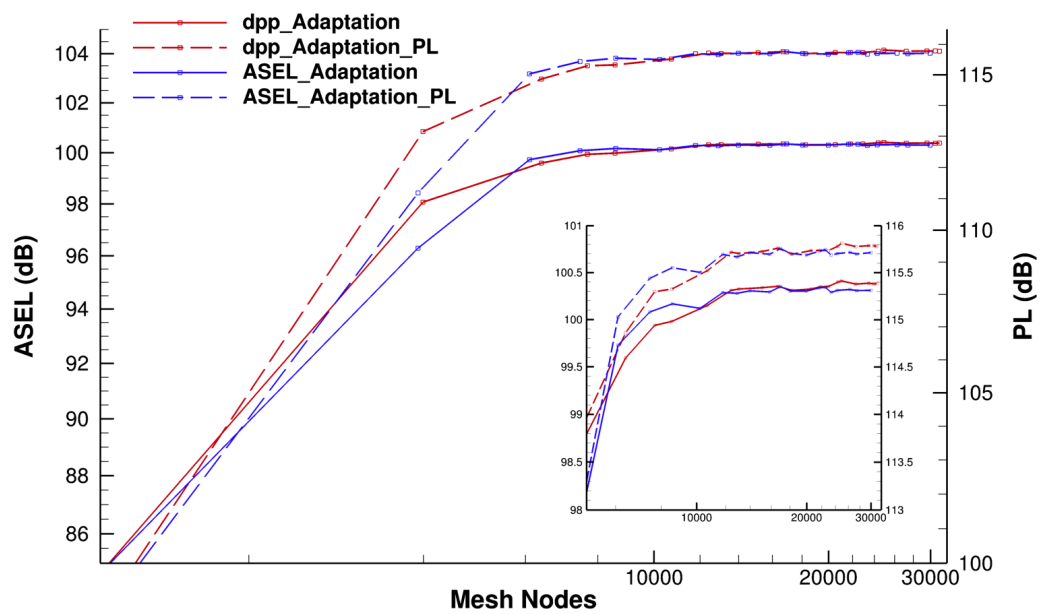
Figure 7. Loudness convergence for both schemes using coarse meshes over a diamond airfoil.
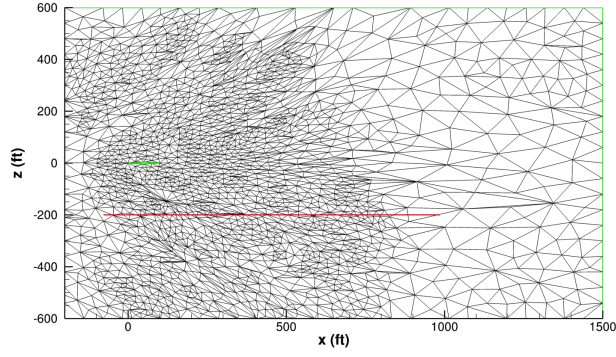
American Institute of Aeronautics and Astronautics
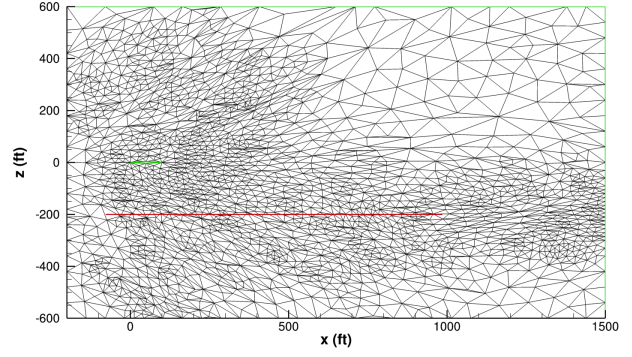
(a) **After the 1st off-body pressure adaptation cycle.**

(b) **After the 1st ASEL adaptation cycle.**
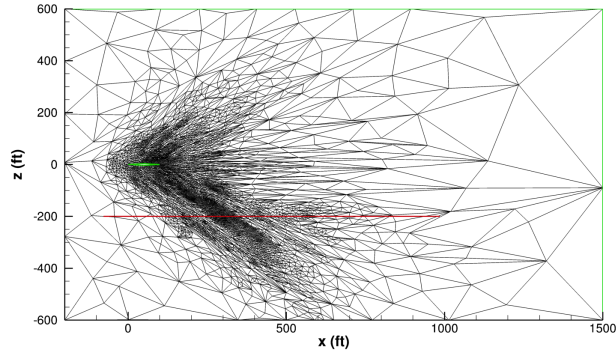
(c) **After the 5th off-body pressure adaptation cycle.**
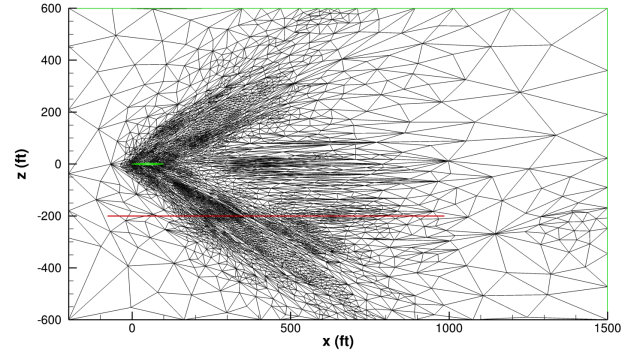
(d) **After the 5th ASEL adaptation cycle.**
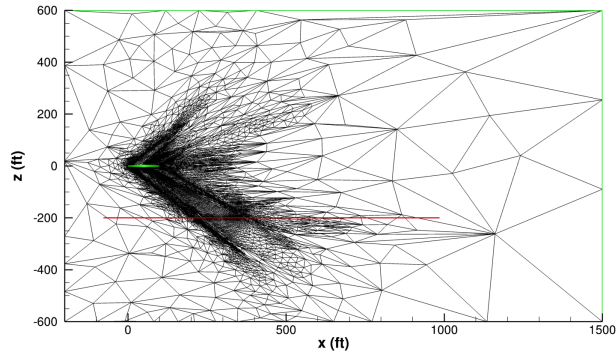
(e) **After the 10th off-body pressure adaptation cycle.**
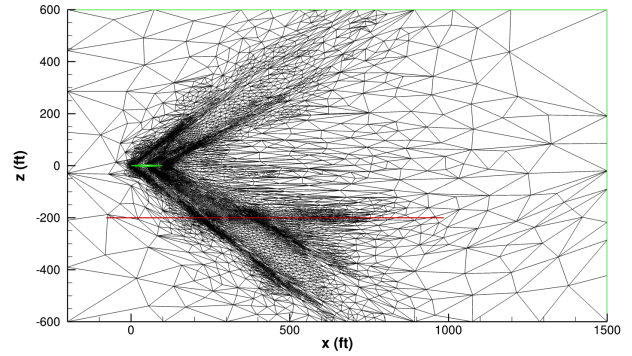
(f) **After the 10th ASEL adaptation cycle.**
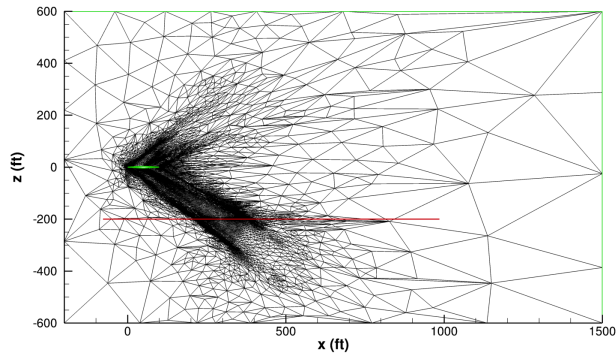
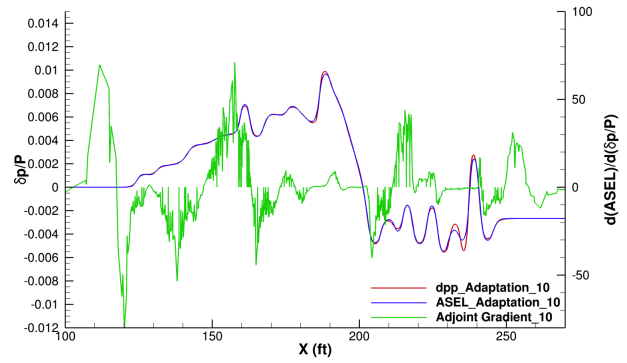(g) **After the 20th off-body pressure adaptation cycle.**
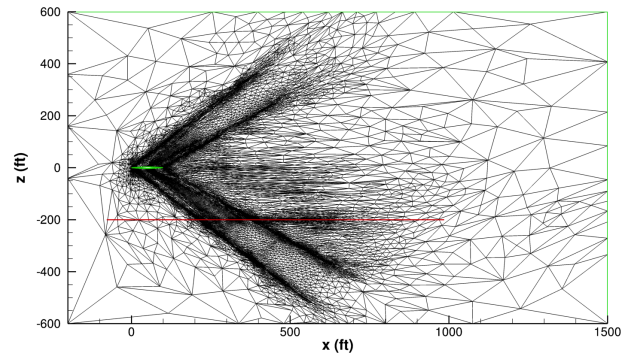
(h) **After the 20th ASEL adaptation cycle.**

Figure 8. Grid changes during adjoint-based mesh adaptation over a diamond airfoil using coarse meshes.

American Institute of Aeronautics and Astronautics
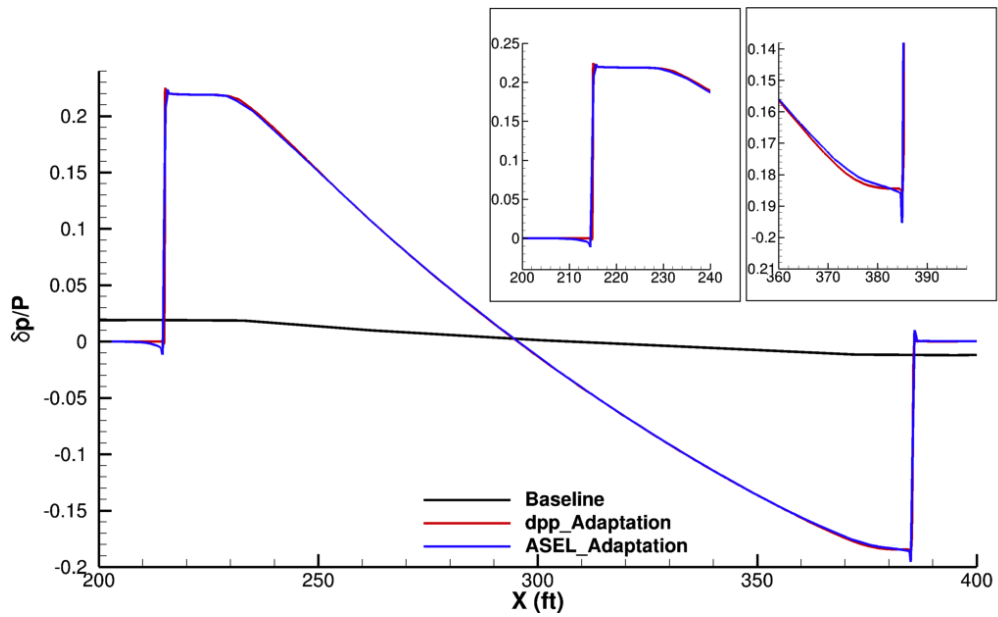
Figure 9. Comparison of near-field waveforms.
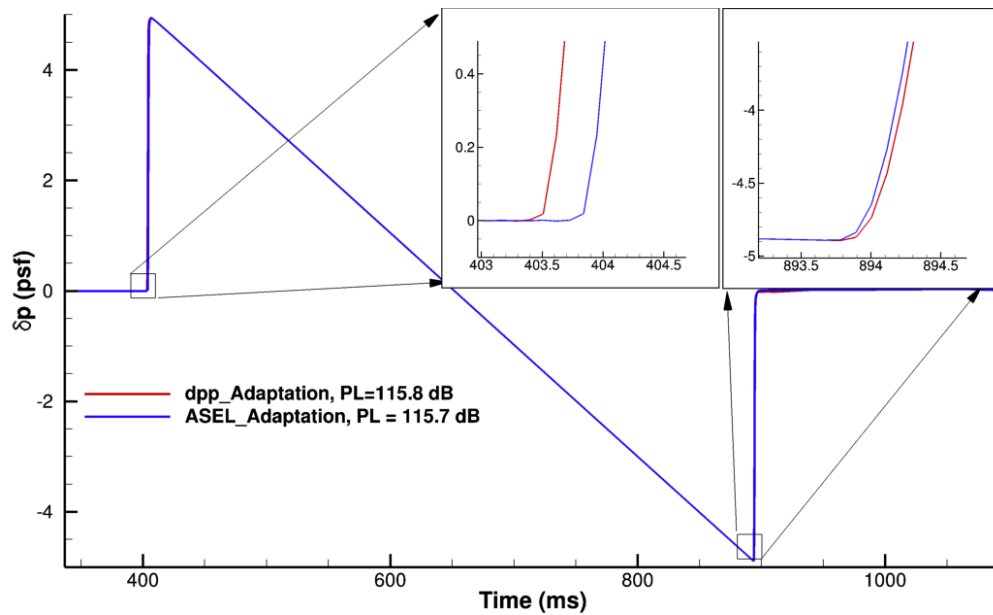
Figure 10. Comparison of ground signatures.

American Institute of Aeronautics and Astronautics
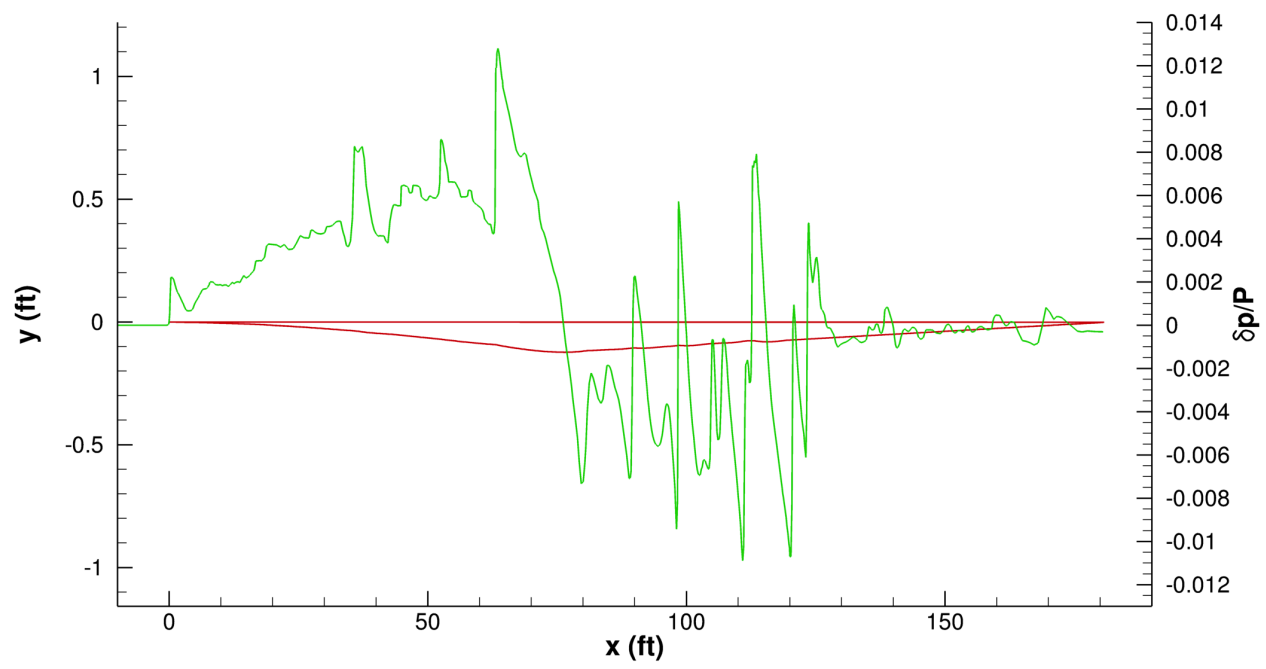
Figure 11. Desired near-field pressure waveform and corresponding airfoil.
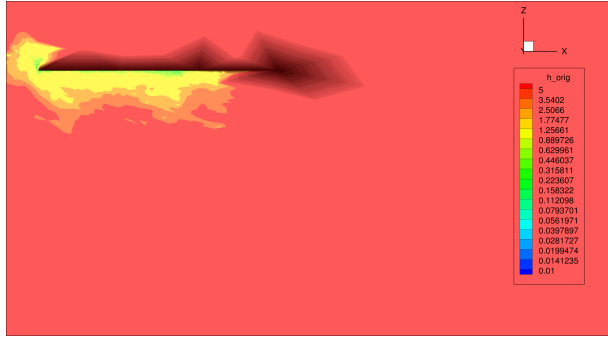
American Institute of Aeronautics and Astronautics

(a) **After the 1st off-body pressure adaptation cycle.**

(b) **After the 1st ASEL adaptation cycle.**
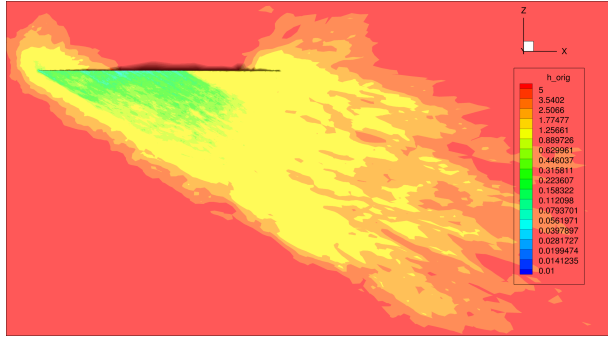
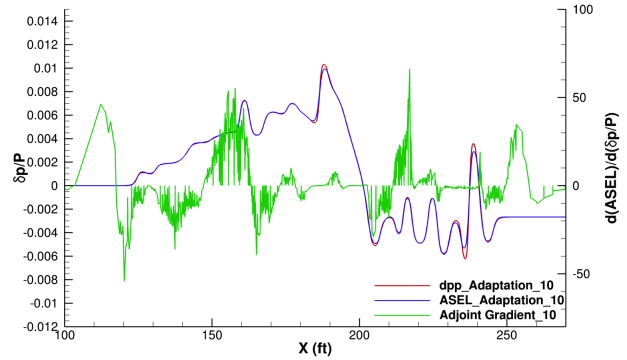(c) **After the 5th off-body pressure adaptation cycle.**

(d) **After the 5th ASEL adaptation cycle.**

(e) **After the 10th off-body pressure adaptation cycle.**

(f) **After the 10th ASEL adaptation cycle.**

(g) **After the 20th off-body pressure adaptation cycle.**

(h) **After the 20th ASEL adaptation cycle.**

Figure 12. Cell size contours during mesh adaptation for complex 2D simulation.
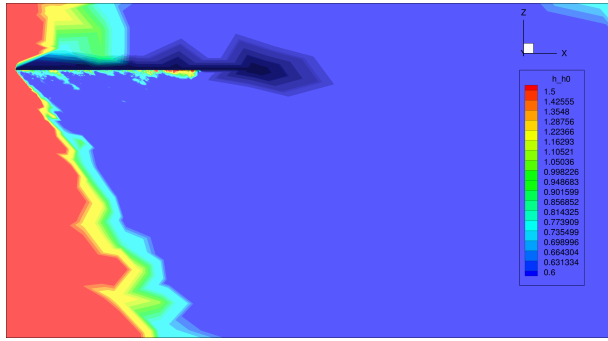
American Institute of Aeronautics and Astronautics

(a) **After the 1st off-body pressure adaptation cycle.**

(b) **After the 1st ASEL adaptation cycle.**
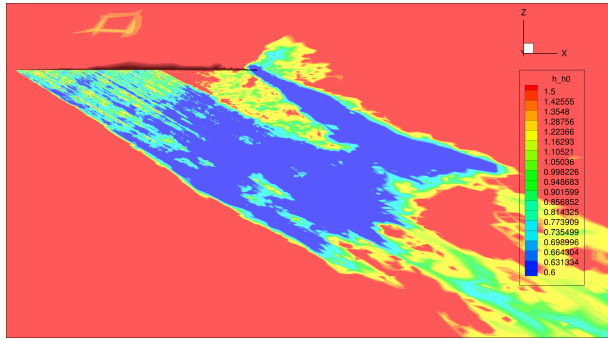
(c) **After the 5th off-body pressure adaptation cycle.**

(d) **After the 5th ASEL adaptation cycle.**

(e) **After the 10th off-body pressure adaptation cycle.**

(f) **After the 10th ASEL adaptation cycle.**

(g) **After the 20th off-body pressure adaptation cycle.**

(h) **After the 20th ASEL adaptation cycle.**

Figure 13. Cell size projection contours during mesh adaptation for complex 2D simulation.
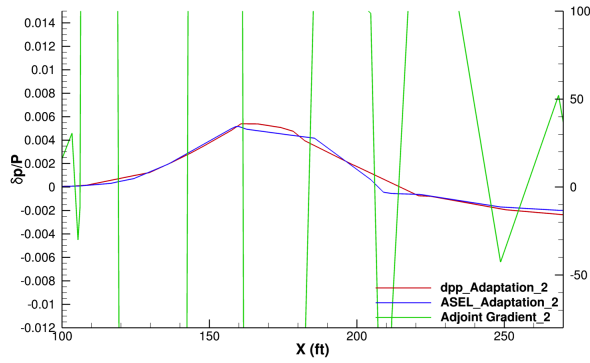
American Institute of Aeronautics and Astronautics

(a) **After the 1st off-body pressure adaptation cycle.**

(b) **After the 10th off-body pressure adaptation cycle.**
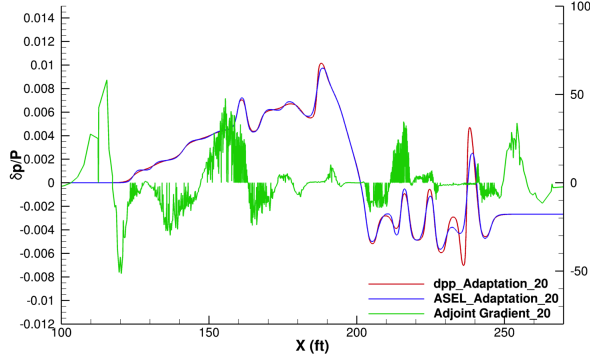
(c) **After the 20th off-body pressure adaptation cycle.**
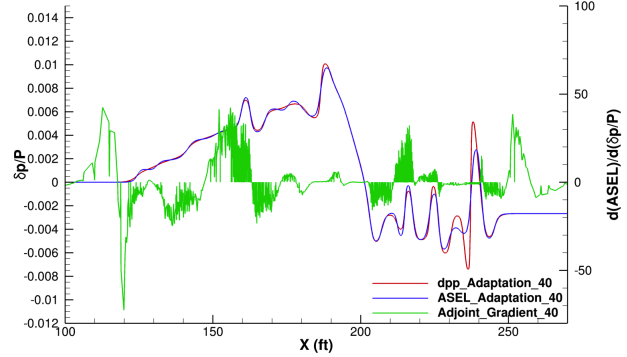
(d) **After the 40th off-body pressure adaptation cycle.**

**Figure 14. Differences during mesh adaptation for complex 2D simulation using moderate refinement.**
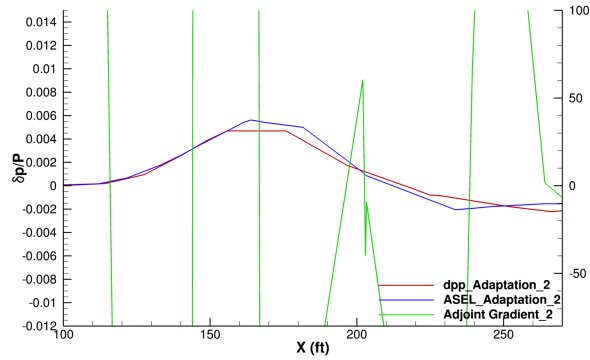
(a) **After the 1st off-body pressure adaptation cycle.**

(b) **After the 10th off-body pressure adaptation cycle.**
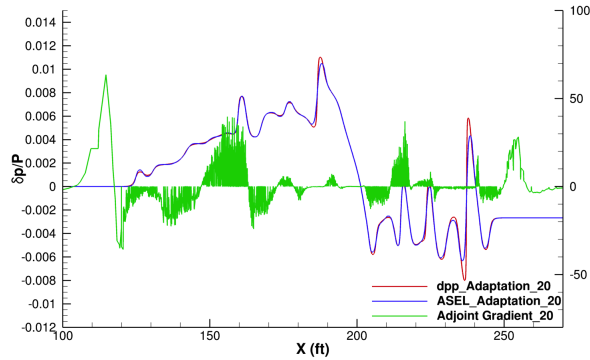
(c) **After the 20th off-body pressure adaptation cycle.**
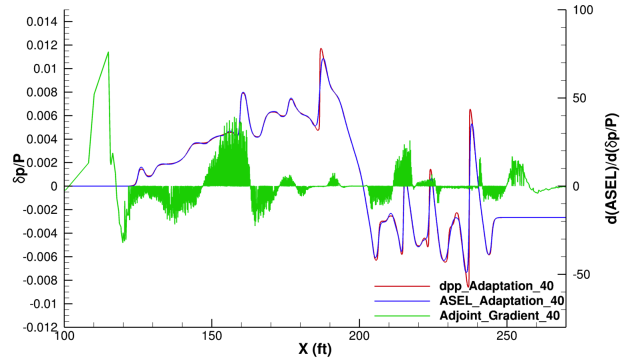
(d) **After the 40th off-body pressure adaptation cycle.**

Figure 15. Differences during mesh adaptation for complex 2D simulation using high refinement.

American Institute of Aeronautics and Astronautics
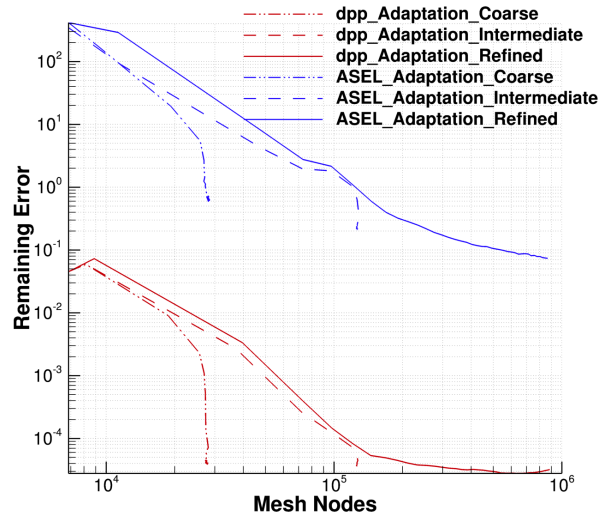
(a) Remaining error convergence.
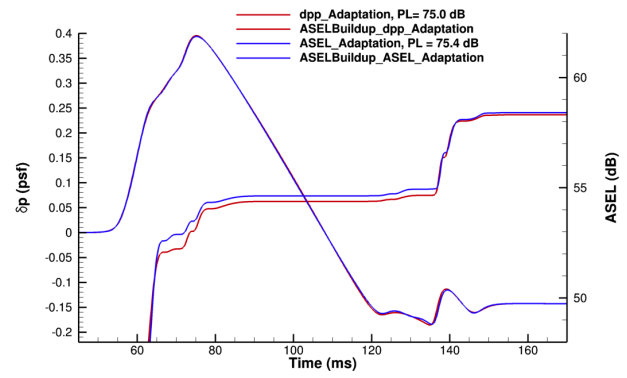
(b) Ground signatures after 40th adaptation cycle using a coarse mesh.
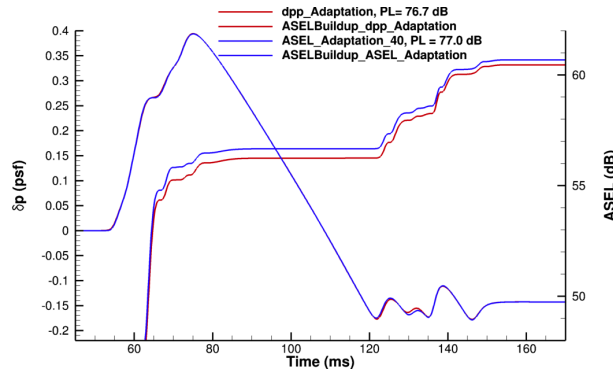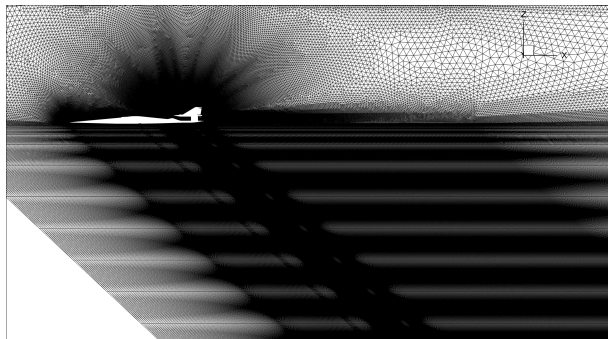

(c) Ground signatures after 40th adaptation cycle using a moderately refined mesh.
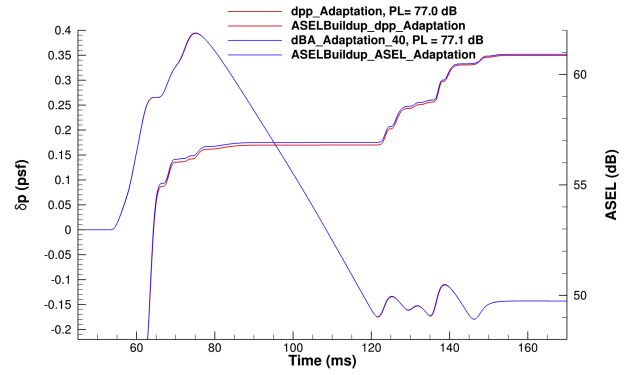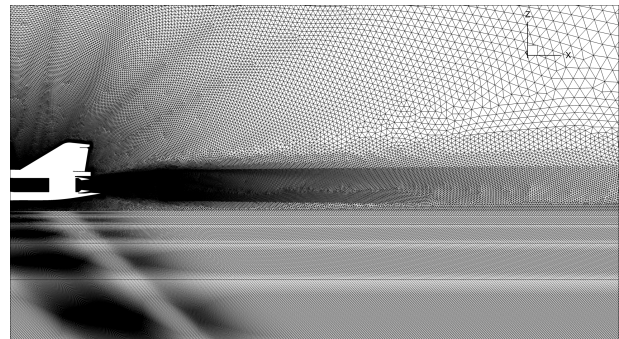

(d) Ground signatures after 40th adaptation cycle using a refined mesh.

Figure 16. Mesh convergence and ground signatures from different meshes for a complex 2D simulation

(a) Below the vehicle.

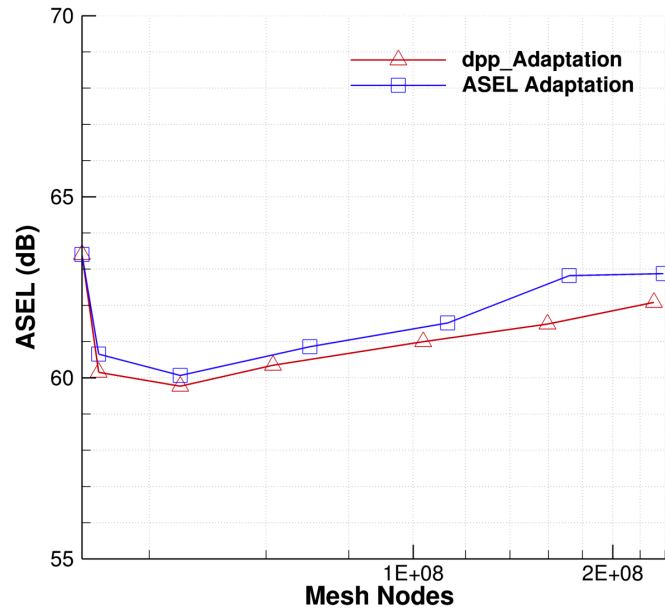(b) Aft of the vehicle.

Figure 17. Baseline mesh over a representative low boom concept.
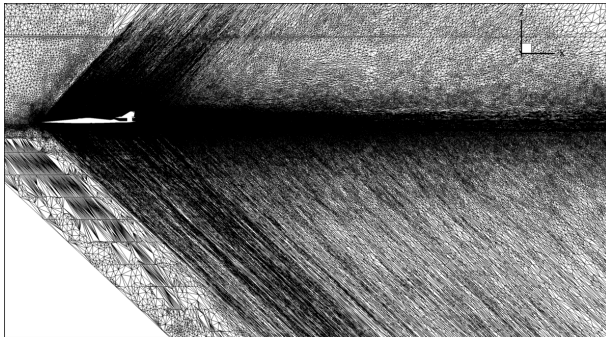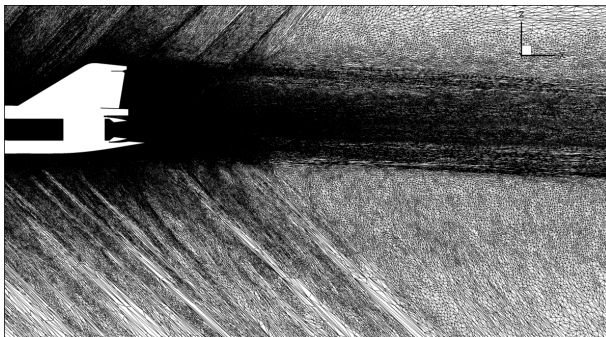
American Institute of Aeronautics and Astronautics

Figure 18. ASEL loudness convergence for the low boom concept.
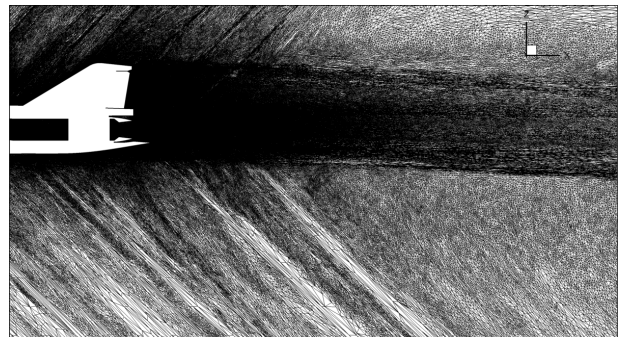

(a) **Overall mesh after 8 off-body pressure adaptation cycles.**

(b) **Overall mesh after 8 ASEL adaptation cycles.**

(c) **Aft mesh using off-body pressure adaptation.**

(d) **Aft mesh using ASEL adaptation.**

Figure 19. Adapted aft meshes over the low boom concept.

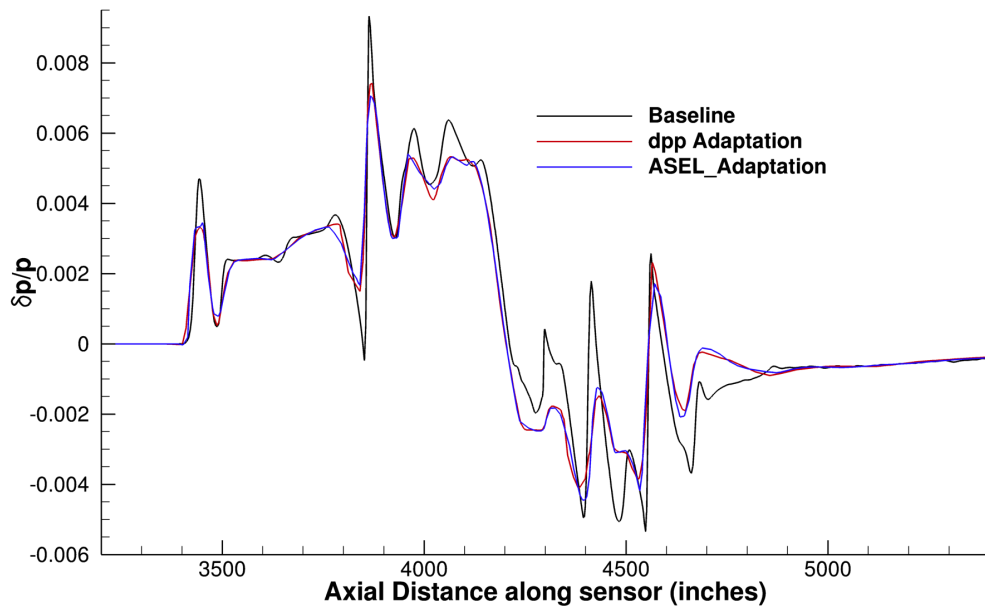American Institute of Aeronautics and Astronautics

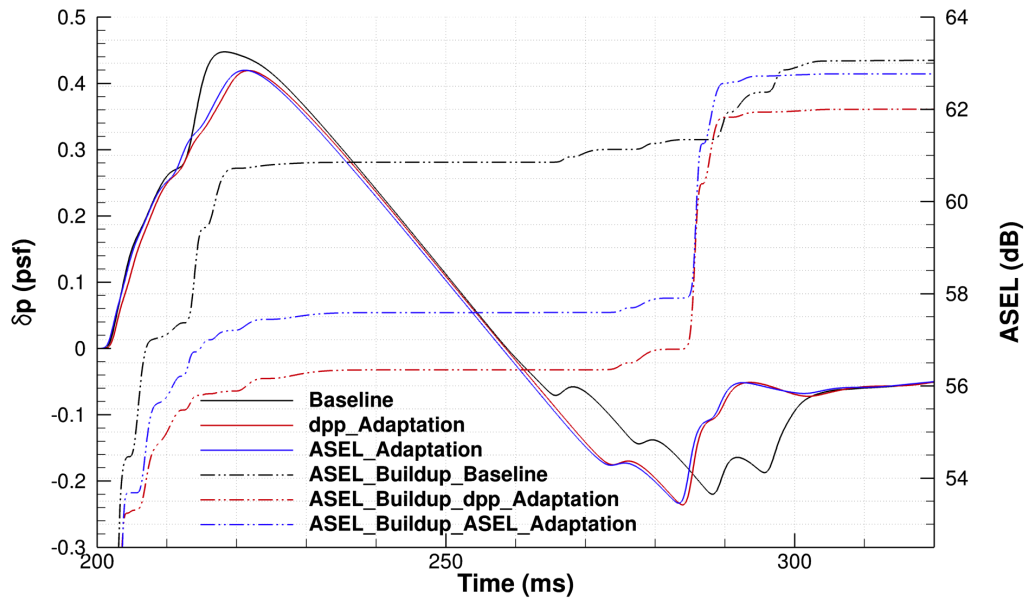**Figure 20. Near-field pressure waveform comparison for the low boom concept.**

Figure 21. Ground signature comparison for the low boom concept.

American Institute of Aeronautics and Astronautics